



## PAPER

# Structural defects in Fe–Pd-based ferromagnetic shape memory alloys: tuning transformation properties by ion irradiation and severe plastic deformation

To cite this article: S G Mayr and A Arabi-Hashemi 2012 *New J. Phys.* **14** 103006

View the [article online](#) for updates and enhancements.

## Related content

- [Mechanical properties and twin boundary drag in Fe–Pd ferromagnetic shape memory foils—experiments and ab initio modeling](#)

I Clausen and S G Mayr

- [Ion-irradiation-assisted tuning of phase transformations and physical properties in single crystalline Fe<sub>7</sub>Pd<sub>3</sub> ferromagnetic shape memory alloy thin films](#)

A Arabi-Hashemi, R Witte, A Lotnyk et al.

- [Simulating functional magnetic materials on supercomputers](#)

Markus Ernst Gruner and Peter Entel

## Recent citations

- [Thermal and structural properties of the martensitic transformations in Fe<sub>7</sub>Pd<sub>3</sub> shape memory alloys: an \*ab initio\*-based molecular dynamics study](#)

Alexander Holm and Stefan G Mayr

- [Ion-irradiation-assisted tuning of phase transformations and physical properties in single crystalline Fe<sub>7</sub>Pd<sub>3</sub> ferromagnetic shape memory alloy thin films](#)

A Arabi-Hashemi *et al*

- [Bulk and surface properties of Co–Fe and Fe–Pd liquid alloys](#)

R.P. Koirala *et al*

## Structural defects in Fe–Pd-based ferromagnetic shape memory alloys: tuning transformation properties by ion irradiation and severe plastic deformation

S G Mayr<sup>1,2,3</sup> and A Arabi-Hashemi<sup>1</sup>

<sup>1</sup> Leibniz-Institut für Oberflächenmodifizierung e.V., Permoserstrasse 15, D-04318 Leipzig, Germany

<sup>2</sup> Translationszentrum für Regenerative Medizin und Fakultät für Physik und Geowissenschaften, Universität Leipzig, Germany

E-mail: [stefan.mayr@iom-leipzig.de](mailto:stefan.mayr@iom-leipzig.de)

*New Journal of Physics* **14** (2012) 103006 (18pp)


Received 6 June 2012

Published 2 October 2012

Online at <http://www.njp.org/>

doi:10.1088/1367-2630/14/10/103006

**Abstract.** Fe–Pd-based ferromagnetic shape memory alloys constitute an exciting class of magnetically switchable smart materials that reveal excellent mechanical properties and biocompatibility. However, their application is severely hampered by a lack of understanding of the physics at the atomic scale. A many-body potential is presented that matched *ab initio* calculations and can account for the energetics of martensite ↔ austenite transition along the Bain path and relative phase stabilities in the ordered and disordered phases of Fe–Pd. Employed in massively parallel classical molecular dynamics simulations, the impact of order/disorder, point defects and severe plastic deformation in the presence of single- and polycrystalline microstructures are explored as a function of temperature. The model predictions are in agreement with experiments on phase changes induced by ion irradiation, cold rolling and hammering, which are also presented.

 Online supplementary data available from [stacks.iop.org/NJP/14/103006/mmedia](http://stacks.iop.org/NJP/14/103006/mmedia)

<sup>3</sup> Author to whom any correspondence should be addressed.

**Contents**

<b>1. Introduction</b>	<b>2</b>
<b>2. Construction of an embedded atom method potential for Fe–Pd</b>	<b>3</b>
<b>3. Influence of order/disorder on phase stability</b>	<b>6</b>
<b>4. Point defects</b>	<b>9</b>
<b>5. Severe plastic deformation</b>	<b>10</b>
<b>6. Comparison with experiments and discussion</b>	<b>14</b>
6.1. 1.8 MeV Kr <sup>+</sup> irradiation of austenitic single-crystal Fe <sub>7</sub> Pd <sub>3</sub> films . . . . .	14
6.2. Severe plastic deformation of Fe <sub>7</sub> Pd <sub>3</sub> splats . . . . .	16
<b>7. Conclusions and outlook</b>	<b>16</b>
<b>Acknowledgments</b>	<b>17</b>
<b>References</b>	<b>17</b>

**1. Introduction**

Since their discovery in the mid-1990s [1], magnetic shape memory (MSM) alloys have attracted much scientific interest owing to a broad range of conceivable engineering applications and highly interesting underlying physics related to the coupling between structural, mechanical, magnetic and thermodynamic properties (see, e.g., [2] and references therein for a recent perspective). Besides off-stoichiometric Ni<sub>2</sub>MnGa Heusler alloys [3], alternative materials systems with complementary properties have also become attractive more recently, including Fe<sub>7+ $\delta$</sub> Pd<sub>3- $\delta$</sub>  ( $|\delta| \lesssim 0.2$ ) [4] alloys due to their higher ductility, better corrosion resistance and excellent biocompatibility [5]. Mediated by reorientation of martensite variants via twin boundary motion, the prevalence of the face centered tetragonal (fct) martensitic phase with a minimum of lattice defects at the operation temperature is a precondition for the occurrence of the MSM effect—as only this phase has been established to reveal high enough magnetic anisotropies and twin boundary mobilities [6]. Although fct martensite can be obtained when cooling fcc austenite through the martensite transition, further irreversible transformation into competing body central tetragonal (bct) and cubic (bcc) martensites needs to be prevented by an appropriate choice of compositions and processing conditions ([7] and references therein). It is worth emphasizing that for the present alloy austenite as well as all martensite phases are ‘random’ solid solutions, which originate from the equilibrium high-temperature  $\gamma$  phase by a sufficiently rapid cooling to prevent decomposition into L1<sub>0</sub> FePd and bcc Fe.

Although macroscopically of ‘random’ nature, recent conversion electron Mößbauer spectroscopy measurements on sufficiently relaxed splats have unveiled ordering tendencies, namely a preference for Fe–Pd coordination [8]. As density functional theory (DFT) calculations indicate severe impact of the degree and nature of disorder on the potential and free energy landscapes between the bcc, bct, fct and fcc phases [9–11], ordering tendencies have to be expected to leave their mark on (inter)martensite transformations. Although direct experimental corroboration of these concepts is—to our knowledge—unavailable at this point, the significant scattering of experimental data in the literature on the martensite  $\leftrightarrow$  austenite transition temperatures as a function of stoichiometry and preparation conditions might indirectly account for this. Another at least equally significant aspect as atomic disorder refers

to (i) intrinsic and (ii) extrinsic lattice defects that—as per definition—reside in and out of thermal equilibrium, respectively. Surrounded by strain and stress fields, the latter will certainly leave their marks on the martensite  $\leftrightarrow$  austenite transition, as the shear stress fields within austenite have been demonstrated, e.g., to shift the martensite temperature, as described by the Clausius–Clapyron equation [12]. With respect to phase transformation kinetics, on the other hand, lattice defects are well established to act as nuclei—in particular for transformation from austenite to martensite [13], while—within martensite—their enthalpy can be largely reduced by the martensite adaptive nature that allows for stress field reduction (which also relates to the defect-induced shift of phase transition temperature discussed above).

The above considerations make clear that a significantly better understanding of the impact of order/disorder and defects on Fe–Pd-based MSM alloys is highly desirable—in the first place due to their intrinsic presence, but vice versa as a tool for fine-tuning properties. In fact, as strategies for increasing martensite temperature significantly above room or body temperature are highly desirable and the addition of a third component has largely failed to achieve this goal, modification of order/disorder or tailored insertion of defects might be the approach of choice. This is particularly true when heading for biomedical applications of Fe–Pd-based alloys, where the addition of metallurgically suitable elements might be at odds with the requirements of biocompatibility. The latter aspect constitutes the basis from an application point of view for our present study to investigate the impacts of (i) disorder/order, (ii) insertion of point defects and (iii) severe plastic deformation (SPD) on the relative stability of the martensite and austenite phases. This would enable convenient tuning with well-established techniques, namely ion bombardment (i) and (ii) and cold rolling (iii).

For a complete understanding and due to the complexity of the problem, we employ a combined computational–experimental approach in the following. While experimentally we use the standard techniques of ion irradiation and cold rolling/hammering in the following, the greatest challenge on the modeling side is the lack of a suitable empirical potential to allow for large-scale atomistic simulations. Atomistic modeling approaches for Fe–Pd employed DFT calculations [9–11]. Although they have already been performed on state-of-the-art supercomputers, they are incapable of dealing realistically with many aspects of order/disorder, defects and thermodynamics due to severe size limitations on the feasible simulation cells. The modeling part of the present paper consequently will first report about a fitting approach of an empirical embedded atom method (EAM) [14, 15] for Fe–Pd to match the energetics of the Bain path between the disordered austenite ( $\gamma$ ) and martensite phases. We aim to correctly describe the austenite  $\leftrightarrow$  martensite transformation, as well as correctly account for the relative stabilities of the ordered  $L1_0$  and  $L1_2$  phases, as predicted by DFT calculations. This potential is subsequently applied to study the atomistics underlying the impact of order/disorder and defects on martensite  $\leftrightarrow$  austenite transformation—as a counterpart of the experimental studies.

## 2. Construction of an embedded atom method potential for Fe–Pd

DFT [16]-based total energy calculations were employed to determine the ground state energies of representative configurations objectively considered to be of particular importance within the present study. Electronic structure calculations employed ultrasoft pseudopotentials [17, 18] based on the atomic reference configurations [Ar]  $3d^74s^1$  and [Kr]  $4d^95s^1$  for Fe and

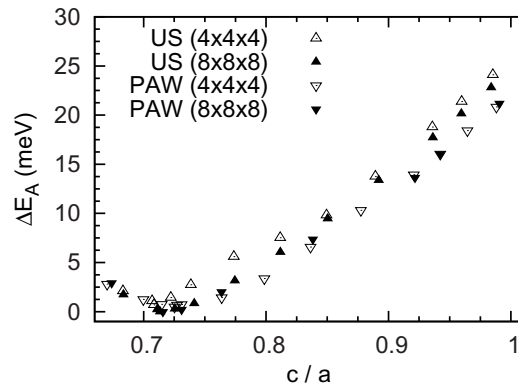


**Figure 1.** DFT predictions for the ground state energy per atom,  $E_A$ , along the Bain path for disordered  $\text{Fe}_{71.25}\text{Pd}_{28.75}$ , employing ultrasoft pseudopotentials (US) and the project-augmented wave (PAW) approach (data from [11]). The degree of tetragonality is characterized by  $c/a$  choosing austenite as the reference structure.

Pd, respectively<sup>4</sup>, that were demonstrated to yield excellent agreement with a complementary PAW approach [19] in a recent work [11], and a plane-wave basis set, as implemented in the pwscf code [20]. The effects of exchange and correlation were treated according to the Perdew–Burke–Ernzerhof functional [21] with spin-polarized generalized gradient correction. To incorporate disorder effects most realistically, a special quasirandom structures (SQS) approach [22] was employed to include ionic relaxations relative to the ‘theoretical’ (that is, perfect) lattice. In doing so—we intrinsically pay the price of having to compromise between computationally challenging large cells and less flexibility in choosing the composition; we therefore decided to stick to the stoichiometry,  $\text{Fe}_{71.25}\text{Pd}_{28.75}$ , in the following due to the availability of reasonably sized well-studied supercells of 32 atoms [23]. For the ordered  $L1_0$  and  $L1_2$  phases, as well as pure fcc Pd and fcc Fe, simple cubic unit cells with four basis atoms were employed, while for bcc Fe the corresponding simple cubic unit cells with a two-atom basis were utilized. Brillouin zone integration (using  $8 \times 8 \times 8$  and  $32 \times 32 \times 32$   $\Gamma$ -centered meshes for SQS and non-SQS cells, respectively) using Methfessel–Paxton smearing [24] (0.2 eV), as well as energy cutoff of the plane-wave basis set (476.2 eV) and augmentation charges (4762 eV) were optimized to obtain energy convergence better than 0.5 meV per atom after structural relaxation runs. Within the present study, ionic and cell relaxations are always realized with the Broyden–Fletcher–Goldfarb–Shanno (BFGS) scheme as implemented in pwscf.

Figure 1 shows the dependence of the ground state energy along the Bain path ranging from bcc martensite ( $c/a = 0.707$ ) to austenite ( $c/a = 1.0$ ), which is characterized by a very shallow energy landscape with a global minimum deep within the martensitic state close to bcc martensite. Here the direction of tetragonality (i.e. the  $c$ -axis) was chosen parallel to the  $y$ -direction of the SQS cell proposed in [23], as the other two orientations of the  $c$ -axis (in the  $x$ - and  $y$ -directions of the SQS cell) yield elevated energies upon ionic relaxations due to the formation of nanotwins [11]. It is worth pointing out that these results are in excellent quantitative agreement with complementary studies using the same SQS cell, but using the PAW approach, different exchange functionals, diagonalization and ionic relaxation

<sup>4</sup> Pseudopotential files Fe.pbe-nd-rrkjus.UPF and Pd.pbe-rrkjus.UPF are available at <http://www.pwscf.org>.

**Table 1.** Comparison between DFT and EAM predictions for enthalpies of mixing,  $\Delta H_m$ , and lattice constants ( $\langle a + b \rangle$  and  $c$ ) of the tetragonal unit cell.

	$\Delta H_m$		$\langle a + b \rangle$		$c$	
	DFT	EAM	DFT	EAM	DFT	EAM
bcc Fe	–	–	2.85	2.85	2.85	2.85
fcc Fe	–	–	3.57	3.66	3.57	3.66
fcc Pd	–	–	3.97	3.97	3.97	3.97
L1 <sub>2</sub> Fe <sub>3</sub> Pd	0.080	0.155	3.72	3.90	3.73	3.90
L1 <sub>0</sub>	–0.101	–0.041	3.77	3.82	3.87	3.82
L1 <sub>2</sub> FePd <sub>3</sub>	–0.128	–0.186	3.91	3.77	3.91	3.77

algorithms [9, 11], which confirms the independence of implementation details. As the particular focus within the present work is on the austenite  $\leftrightarrow$  martensite transition, figure 1 will play a central role in our coarse-graining approach, namely the adjustment of an empirical EAM potential to correctly account for the austenite  $\leftrightarrow$  martensite transformation. Additional ‘target’ parameters taken from DFT include the enthalpies of mixing,  $\Delta H_m$ , of the L1<sub>0</sub> and L1<sub>2</sub> phases relative to bcc Fe/fcc Pd and each other, as well as the degrees of tetragonality as given by  $c/a$ . DFT predictions for these key properties are included in table 1.

As the cohesive model we write for the energy of an atom system

$$E = \frac{1}{2} \sum_{\substack{i,j \\ i \neq j}}^n \phi_{t_i,t_j}(r_{ij}) + \sum_i^n F_{t_i}(\hat{\rho}_i), \quad (1)$$

where  $\phi_{t_i,t_j}(r_{ij})$  describes the pair interaction between two atoms ( $i, j$ ) of types  $t_i$  and  $t_j$ , which are separated by distance  $r_{ij}$ , and  $F_{t_i}(\hat{\rho}_i)$  denotes the embedding function for an atom of type  $t_i$ , which depends on site electron density,  $\hat{\rho}_i$ . The latter includes contributions  $\rho_{t_j}(r_{ij})$  from all other atoms  $j$  of the system and thus is calculated as

$$\hat{\rho}_i = \sum_{\substack{j \\ j \neq i}}^n \rho_{t_j}(r_{ij}). \quad (2)$$

For a binary system, therefore, in total seven functions—three pair interactions, two embedding functions and two electron densities—need to be defined. We decided to rely for a description of the Fe–Fe interaction on the well-tested parameterization by Mendeleev *et al* [25], while we initially based the Pd–Pd interaction on the well-tested Voter and Chen Ni–Ni potential [26], which was subsequently rescaled in space and energy to match the lattice spacing and cohesive energy predicted by DFT. In fact, in the course of our overall potential fitting, the latter approach proved to be superior to employing the original Pd–Pd potential proposed by the same authors [27]. The subsequent setting up of the Fe–Pd cross-potential was inspired by a recent work on Fe–Ni by Bonny *et al* [28] and consisted of (i) setting up a spline table from scratch for  $\phi_{\text{Fe-Pd}}(r)$  and (ii) re-gauging the constructed Pd potential—relative to Fe—following the recipe proposed by Voter and Chen [26]. As (i) and (ii) are coupled, fitting consisted of successive adjustments to the target values (in the first place the energetics of

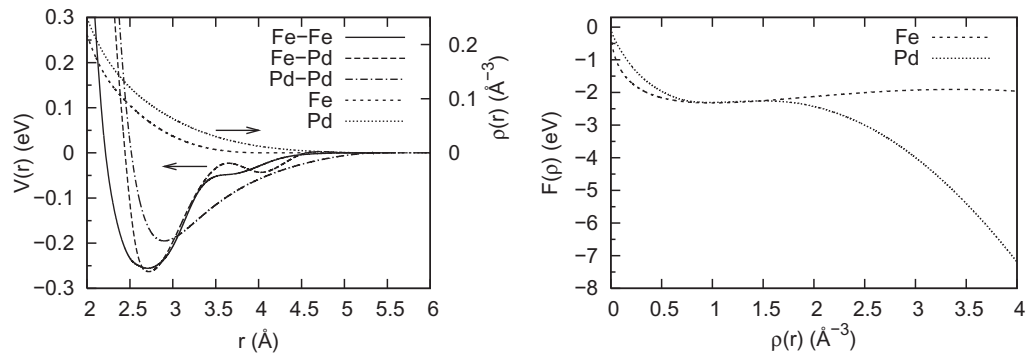


**Figure 2.** Pairwise interaction  $V(r)$ , electron density  $\rho(r)$  and embedding energy  $F(\rho)$  functions constituting the Fe–Pd potential.

the Bain path—figure 1, but also table 1) in several tens of adjustment cycles; the final spline tables of all seven functions are included in the supplementary materials (available from [stacks.iop.org/NJP/14/103006/mmedia](http://stacks.iop.org/NJP/14/103006/mmedia)) of this paper and are plotted in figure 2.

While agreement, transferability, prediction of properties and comparison to experiments will be the focus of the rest of this paper, table 1—for convenience—already includes a comparison between DFT and EAM with respect to elemental as well as ordered  $L1_0$  and  $L1_2$  phases. It is worth emphasizing here that reproduction of the correct enthalpies of mixing and tetragonality are at the center of the applied fitting strategy—while exact reproduction of lattice parameters was not targeted. Clearly, the aim of obtaining the correct relative stabilities of the relevant phases is achieved, while deviations in the lattice parameter are less than 5%.

### 3. Influence of order/disorder on phase stability

As recent conversion electron Mößbauer spectroscopy measurements on splats indicate short-range ordering tendencies in favor of Fe–Pd coordination in the course of annealing treatment [8] while these ordering tendencies are also expected on thermodynamic grounds (similarly to the Fe–Pt system, which reveals an ordered phase in the corresponding region of the phase diagram [29]), our first study with the newly constructed Fe–Pd EAM potential will be devoted to the impact of order/disorder on the Bain path. In fact, from a modeling point of view, detailed understanding of the impact of order/disorder on the transformation characteristics has up to now been severely hampered by the very limited number of atoms feasible in DFT calculations, while indications of a strong influence of the details of ‘disorder’ have been omnipresent: as an example, the energetics along the Bain path calculated within the coherent potential approximation [30] reveals fundamentally different signatures from SQS approaches [9–11], which—again—critically depend, e.g., on the orientation of the SQS cell as well as the absence or presence of ion relaxation. Deviations between DFT predictions and experimental observations might strongly hint at less disorder within experimental Fe–Pd than mimicked by SQS cells (see [11] and references therein for a more detailed discussion of this point). Employing the currently constructed Fe–Pd EAM potential in classical molecular dynamics (CMD) simulations [31], where systems up to several millions of atoms are state of the art, these problems of insufficiently sized systems and the requirement for SQS cells can be overcome. Other modeling challenges, such as the kinetics



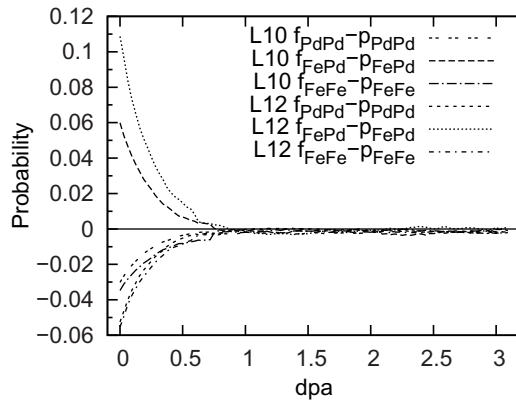


**Figure 3.** The development of short-range order—as characterized by the relative frequencies of atomic pairs  $X$  and  $Y$ ,  $f_{XY}$ —toward the corresponding statistical probabilities,  $p_{XY}$ , namely the random solid solution, in the course of mixing.

of order generation and destruction with decreasing and increasing annealing temperature, respectively, are also clearly beyond the capabilities of CMD—primarily due to the limits on simulation time (some  $\mu\text{s}$  on our infrastructure [32] versus some hours in experiments). Massively parallel CMD simulations were performed with a group-maintained code [33], which solves the classical multiparticle problem for cubically splined EAM potentials with a fifth-order Gear predictor–corrector scheme using an integration time step of 1.52 fs. To allow for thermodynamically meaningful averages, an  $(N, p, T)$  ensemble is realized using the Nosé–Hoover [34, 35] and Parinello–Rahman [36] thermostats and barostats, respectively, while periodic boundaries are applied throughout the rectangular simulation cell. As starting points for our simulations, we choose the fully ordered  $L1_0$   $\text{Fe}_{50}\text{Pd}_{50}$  and  $L1_2$   $\text{Fe}_{75}\text{Pd}_{25}$  phases with  $3.2 \times 10^4$  atoms in total, in which randomly selected Fe and Pd atoms, respectively, are substituted to obtain the desired  $\text{Fe}_7\text{Pd}_3$  stoichiometry; we will term these structures  $\text{Fe}_7\text{Pd}_3\text{-}L1_0$  and  $\text{Fe}_7\text{Pd}_3\text{-}L1_2$ , respectively, in the following. For randomly selected pairs of atoms, the two atoms are each subsequently exchanged. Inspired by ion irradiation-induced exchanges of atoms—and with reference to the experimental section later in this paper—we identify each ‘exchange’ with an atomic ‘displacement’ and thus use ‘displacements per atom’ or ‘dpa’ as the quantification in the following. When starting from greatly ordered  $\text{Fe}_7\text{Pd}_3\text{-}L1_0$  and  $\text{Fe}_7\text{Pd}_3\text{-}L1_2$  structures in which atoms are subsequently exchanged, the latter certainly leaves its mark on the compositions of the neighboring shell of atoms, as shown for the nearest-next neighbor shell in figure 3. For both, the  $\text{Fe}_7\text{Pd}_3\text{-}L1_0$  and  $\text{Fe}_7\text{Pd}_3\text{-}L1_2$  structures, the number of different next neighbors decreases with the number of displacements—in favor of equal neighbors. To study the impact of progressive disordering of the  $\text{Fe}_7\text{Pd}_3\text{-}L1_0$  and  $\text{Fe}_7\text{Pd}_3\text{-}L1_2$  phases on the energy landscape along the Bain path, CMD simulations on the tetragonal deformation of the simulation cell from austenite to martensite were performed at 10 K. After initialization by applying Gaussian velocities and displacements corresponding to a temperature of 10 K to the atoms and subsequent equilibration for 50 ps, the cell is tetragonally deformed along the Bain path, while the average energy per atom,  $E_A$ , was monitored, as shown in figure 4. We would like to note that the speed of cell deformation was chosen low enough to obtain results independent of the cell deformation rate—which basically means that its related time scale is lower than



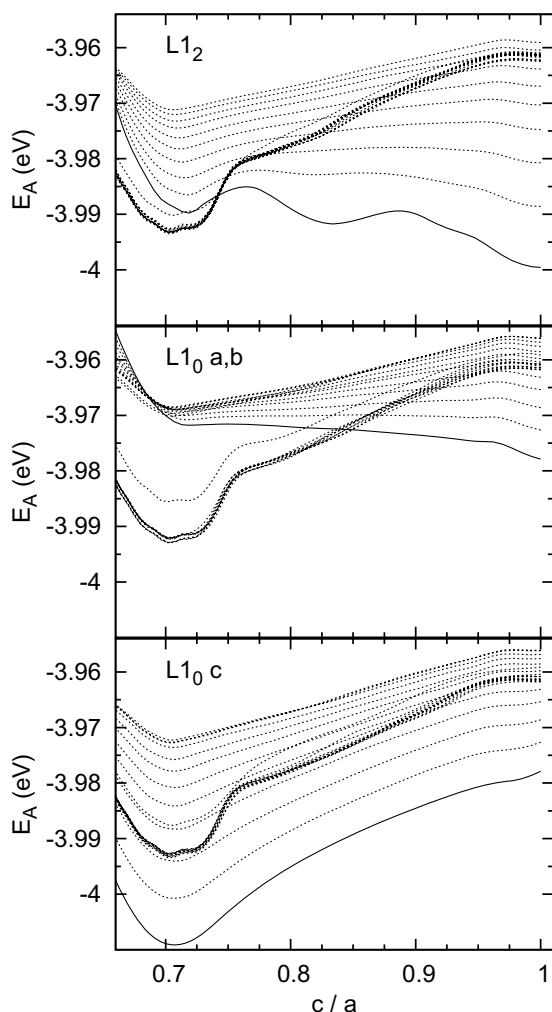


**Figure 4.** Impact of disorder on the ground state energies per atom,  $E_A$ , along the Bain path, as characterized by the tetragonality,  $c/a$ . Starting initially from the ordered  $L1_2$  and  $L1_0$  phases, randomly selected Fe and Pd atoms, respectively, are first exchanged with Pd and Fe, respectively, to yield the desired  $Fe_7Pd_3$  stoichiometry. While the resulting Bain paths (solid lines) are spatially isotropic for the  $L1_2$  phase, the  $a/b$  and  $c$  directions have to be distinguished for the  $L1_0$  phase. Subsequent exchange of randomly selected atom pairs (dashed lines shown in increments of 0.0625 dpa) leads to convergence toward the Bain path of the fully disordered system.

that of phononic vibrations (including soft modes along the martensite  $\leftrightarrow$  austenite transition) or the velocity of sound. From figure 4 it becomes clear that prior to disordering,  $Fe_7Pd_3$ - $L1_0$  and  $Fe_7Pd_3$ - $L1_2$  structures reveal a fundamentally different potential energy landscape with an apparently strong anisotropy between the  $a$ -,  $b$ - and  $c$ -axes for the  $L1_0$ —as expected from its anisotropic crystal structure. Most importantly, the zero-temperature structure of the  $Fe_7Pd_3$ - $L1_2$  and  $Fe_7Pd_3$ - $L1_0$  structures is given by fcc and bcc lattices, respectively. During the first stages of disordering, clearly the energy increases for all configurations, which indicates that a small number of atomic exchanges basically act as defects within the  $Fe_7Pd_3$ - $L1_0$  and

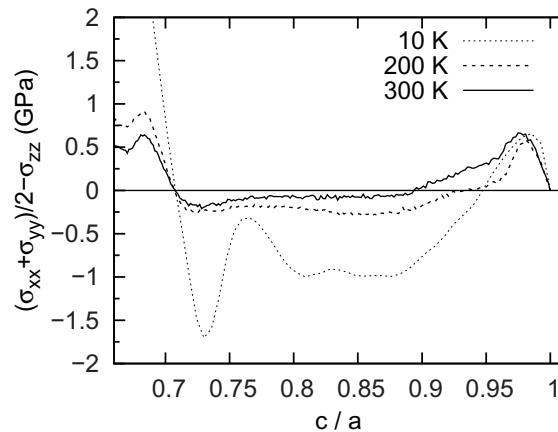


**Figure 5.** Shear stress as a function of tetragonality along the Bain path for the fully disordered cell at different temperatures.

$\text{Fe}_7\text{Pd}_3\text{-L1}_2$  structures. Exceeding  $\approx 0.7$  dpa, disorder apparently becomes so severe that the shape of the potential energy landscape changes fundamentally toward an identical curve independent of the initial configuration, which is characterized by a new minimum occurring close to bcc martensite. As for the temperature dependence of structure, it is instructive to consider the shear stress as a function of tetragonality along the Bain path, which vanishes and reveals a negative slope within (meta) stable equilibrium—as shown for the fully disordered cell in figure 5. Clearly, bcc martensite remains the stable structure throughout the investigated temperature range, which—at first sight—seems at odds with the experimental findings of an fct phase ( $c/a \approx 0.94$ ) at this composition and temperature [6, 37]. However, these findings are no contradiction, but clearly a manifestation of short-range ordering tendencies toward the  $\text{Fe}_{75}\text{Pd}_{25}$   $\text{L1}_2$  phase, as experimentally demonstrated recently [8], which shifts the preferential structure in the fcc direction toward fct. A strong coupling of local order to the austenite  $\leftrightarrow$  martensite transition is, in fact, already included in figure 4. As the ordered  $\text{L1}_2$  and  $\text{L1}_0$  phases reveal lower energy than the disordered phase for  $c/a \gtrsim 0.75$  and  $0.85$ , respectively, the disordered fct and fcc phases can reduce their energies by establishing local order. The potential energy landscape of the experimental austenite  $\leftrightarrow$  martensite transition thus involves a higher dimensional reaction coordinate than the simple Bain  $c/a$  ratio, including the degree of (short-range) order. Kinetic Monte-Carlo simulations, which are currently in progress, will be employed to quantify ordering tendencies from a simulation point of view in future, but are beyond the scope of this work.

Determination of the austenite  $\leftrightarrow$  martensite temperature of fully disordered cells is a highly non-trivial task, as it is well established that during transformation nucleation barriers need to be overcome [13]. For the most accurate determination, we therefore employed a two-phase technique, namely two cells—one in the austenite, the other in the martensite phase at identical temperatures—were prepared and merged crystallographically correctly together. The martensite  $\leftrightarrow$  austenite temperature is identified from a stable (i.e. non-migrating) phase boundary, yielding  $301.0 \pm 0.1$  K.

#### 4. Point defects

Inspired by the capabilities of shear stresses to increase the martensite temperature [12] and motivated by the requirement for room or body (for biomedical applications) temperature stable

martensite, we have been exploring the impact of point defects, which exert an ‘intrinsic’ shear stress on the system and are expected to not interfere severely with twin boundary motion, on phase stability. While vacancies and interstitials can readily be inserted by means of irradiation with energetic ions (see, e.g., [38] for a review), in particular vacancies will certainly also be present to a considerable extent owing to rapid cooling applied during the synthesis of austenite or martensite Fe–Pd. Both aspects are motivation enough to study, in the following, the impact of Frenkel pairs on phase stability in Fe<sub>7</sub>Pd<sub>3</sub> by employing the newly constructed EAM potential.

Starting with a fully disordered austenite cell prepared and characterized with the techniques of section 3, Frenkel pairs are subsequently inserted into the simulation cell basically by removing a randomly selected lattice atom and inserting it at an interstitial site beyond the purely elastic recombination length (see [39] for a detailed description). After a subsequent equilibration run for 50 ps in an  $(N, p, T)$  ensemble at the target temperature  $T$  and zero pressure, the distribution function of the bond angles of an atom with its next neighbors is employed to track down the degree of tetragonality within the system. In tests, the latter, in fact, proved to be a much more sensitive tool than the more commonly used pair distribution function [31]. To ensure comparability with experiments and to cast the results into a higher degree of abstraction, the number of generated Frenkel pairs is normalized to the number of atoms within the cell and thus given in dpa—a measure of dose.

Figures 6(a)–(c) depict the evolution of the angle distribution as a function of dose at different temperatures, which clearly allows us to track down the phase transition to martensite (as visible, e.g., in the bottom and the middle of figures 6(a) and (b), respectively). The systematic evaluation at a broad range of temperatures (figure 6(d)) indicates a linear increase of transition dose with temperature *above* the martensite temperature (301 K—section 3), while severe deviations from linear behavior occur below the martensite temperature. The latter are presumably related to nucleation of the metastable martensite within unstable austenite at these temperatures. The former, on the other hand, is in good agreement with an experimental finding of linear dependence of martensite temperature on externally applied shear stress [12]. As it is perfectly reasonable to assume that each inserted Frenkel pair contributes a shear stress increment on the sample, linear behavior of martensite transition temperature with dose can easily be rationalized and—after all—quantitatively tracked back to the Clausius–Clapyron equation<sup>5</sup>. Evaluation of the dose dependence of martensite temperature within our simulations (figure 6(d)) yields  $(3.95 \pm 0.05) \times 10^{-2}$  dpa K<sup>-1</sup>. Beyond this simple picture, additional contributions are expected from long-range effects and their impact on chemical potential, which affects the stability of martensite versus austenite.

## 5. Severe plastic deformation

As a second test bed for the proposed EAM model for Fe–Pd austenite  $\leftrightarrow$  martensite transition, we address SPD of austenitic Fe<sub>7</sub>Pd<sub>3</sub>, which—besides basic physics—reveals technical relevance in several instances: (i) firstly, similar to ion bombardment, SPD constitutes a well-established technique to introduce defects into materials. In contrast with ion bombardment,

<sup>5</sup> Derivation of the Clausius–Clapyron equation requires thermodynamic equilibrium throughout the system, which at present is not fulfilled owing to large numbers of non-equilibrium defects. We apply it locally in regions that reside in ‘equilibrium’, i.e. between defects. For these regions, defects can be regarded as external boundaries, which impose a constraint (here, a stress state) that affects their transformation behavior.

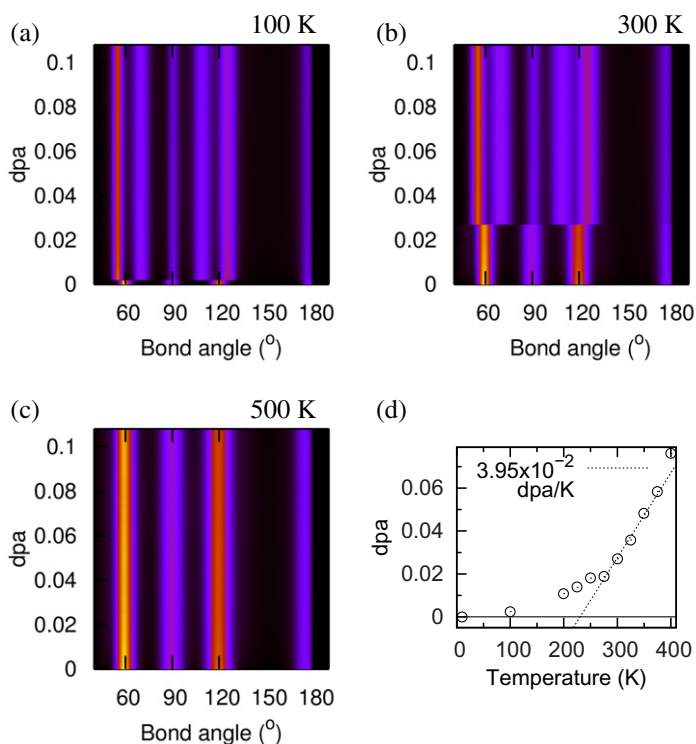


**Figure 6.** Point defect-induced austenite  $\rightarrow$  martensite transition, as observed at different temperatures in the bond angle distribution functions (a)–(c). Above the martensite temperature of the perfect disordered lattice, a linear relation of martensite temperature to defect density is observed (d). The color scales range from dark blue (highest values) to bright yellow (highest values) of the bond angle distribution functions.

however, SPD will certainly affect crystal structure much more severely, so one- or two-dimensional defects are expected. As for the impact on phase stability, with the same arguments as in section 4 an increasing martensite temperature is expected from the stress fields around the defects. (ii) Secondly, SPD is expected to play an important role for fatigue in connection with the long-term use of MSM actuators. In fact, in the course of long-term cycling, SPD will presumably occur in regions of stress concentrations around defects and might herald fatigue by self-enhancement effects. (iii) Thirdly, during the manufacture of MSM actuators, SPD is almost certain to play a central role, as it is implicitly present in several machining techniques. Also from a very practical point of view, a better understanding of the SPD of MSM materials is therefore highly desirable.

Within our computer model, we first realize the SPD of an  $\text{Fe}_7\text{Pd}_3$  austenite single crystal composed of  $3.2 \times 10^4$  atoms in total at variable temperatures and peak strains. Basically, the  $\text{Fe}_7\text{Pd}_3$  austenite single crystal is first relaxed for 50 ps and zero pressure at the desired temperature before performing one cycle of SPD. The latter consists of three consecutive uniaxial extensions and back-contractions subsequently along the  $x$ ,  $y$  and  $z$  directions. Prior to production runs, systematic tests on the strain rates were conducted; it was chosen in such a way as to yield results independent of strain rate, which basically has similar requirements as when

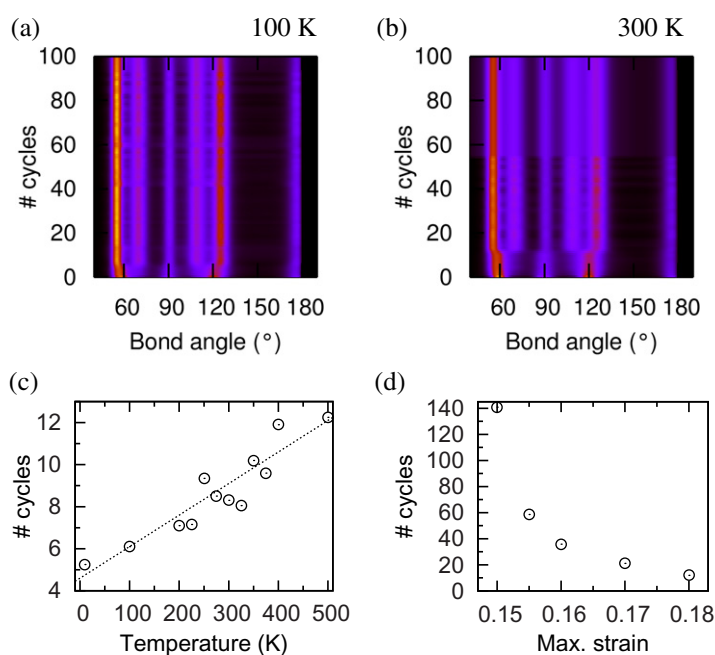


**Figure 7.** Austenite  $\rightarrow$  martensite transformation at different temperatures in the course of SPD as a function of deformation cycles. Clearly detectable from the angle distribution functions (a), (b), the martensite temperature increases approximately linearly as a function of the number of cycles (c). At a fixed temperature—as shown in panel (d) for 300 K—the number of cycles required for inducing austenite  $\rightarrow$  martensite transition increases dramatically with decreasing peak strain. The color scales in (a) and (b) are chosen as in figure 6.

sampling the Bain path (section 3). Every deformation cycle is again followed by a relaxation period of 50 ps and zero stress; after this the angle distribution functions are calculated and the next deformation cycle is performed.

Figures 7(a) and (b) exemplarily depict the evolution of the bond angle distribution as a function of the number of deformation cycles at 100 and 300 K, respectively, at a peak strain of 20%. Clearly, a transformation from austenite to martensite is discernible in the bottom parts of the images. As was systematically evaluated in figure 7(c), the number of cycles required for transformation critically depends on temperature, revealing an approximately linear relationship. This finding can be rationalized based on a decreasing thermodynamic driving force for austenite  $\rightarrow$  martensite transformation at elevated temperatures, which—according to Clausius–Clapyron—consequently requires more defects and thus SPD cycles. Inspection of the simulation cell indicates that these defects are primarily composed of dislocations and deformation twins. The number of cycles dramatically increases with decreasing peak strain during SPD (figure 8(d)); for strains  $\lesssim 15\%$  deformations pretty much occur fully reversible and defect free.

Up to now the impact of SPD on phase stability has only been considered in single crystals. In polycrystalline samples, plastic deformation and accompanying defect generation are expected to occur ‘easier’ or already at lower peak strains applied during cycling, as deformation is expected to occur inhomogeneously with stress and strain concentration in certain portions of the sample. Although aspects such as these including the role of grain

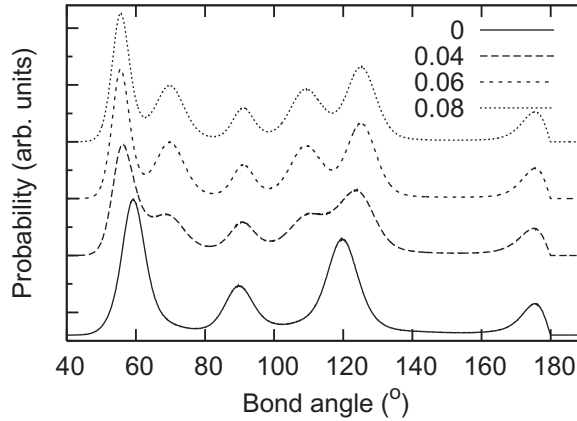


**Figure 8.** Austenite  $\rightarrow$  martensite transformation during a severe plastic deformation of a 6 nm diameter Voronoi polycrystal at  $T = 300$  K: as is visible from the angle distribution function, partial transformation starts to occur already at much lower peak strains than in single crystals (figure 7).

boundaries and grain size has been studied extensively in the mid-2000s (see, e.g., [40] and references therein for a perspective in these years), we at present focus on the impact on phase stability in the  $\text{Fe}_7\text{Pd}_3$  MSM alloy. Employing a Voronoi polycrystal with  $\approx 6$  nm diameter grains and about  $5 \times 10^5$  atoms in total, we determine at a temperature of 300 K the steady-state (that is, limit of infinite deformation cycles) bond angle distributions at different peak strains during cycling (figure 8). Clearly, full transformation to martensite already occurs at peak strains as low as 6%. Partial transformation is already present at peak strains of 4%. This is particularly striking, as in single crystals cycling at strain levels up to 15% has been demonstrated to not affect phase stability (figure 7(d)). We attribute this dramatically different behavior of single and poly-crystals to the relation of external shear direction relative to those crystal orientations that allow for Bain transformations: for the single crystal (figure 7), external shear deformation was compatible with the Bain path: during uniaxial expansion of fcc austenite along one of the  $\langle 100 \rangle$  axes the corresponding strain when fully traversing the Bain path is given by  $2^{(1/6)} - 1 \approx 12\%$ . Up to strain levels as high as that, the single crystal stay morphologically intact (‘pseudoelasticity’ or ‘pseudoplasticity’ [13]). Insertion of defects only starts when exceeding the elastic limit beyond that strain level, namely at  $\approx 15\%$  (figure 7(d)). For the polycrystal, on the other hand, grains are aligned randomly per construction, and thus generally only have strain *components* compatible with possible Bain transformations. As additionally boundary conditions between grains might inhibit transformation along their respective Bain paths, this explains why they are not fully traversed while plastic deformation—accompanied by easy nucleation of full and partial (‘twinning’) dislocations at grain boundaries—begins earlier.

To elucidate where the transformation preferentially occurs in this sample, we employ the structural order parameter,  $P_{\text{st}}(k)$ , of atom  $k$ , as introduced by Zhu *et al* [41]:

$$P_{\text{st}}(k) = \sqrt{\frac{\sum_i (\theta_k(i) - \theta_k^{\text{p}}(i))^2}{\sum_i (\theta_k^{\text{u}}(i) - \theta_k^{\text{p}}(i))^2}}. \quad (3)$$

Here,  $\theta_k(i)$  denotes the  $i$ th smallest angle formed with atom  $k$  at the vertex and its two neighbor atoms,  $\theta_k^{\text{p}}$  is the same quantity for the perfect lattice and  $\theta_k^{\text{u}}(i) = (2\pi i)/(n_{\text{nb}}(n_{\text{nb}} - 1))$



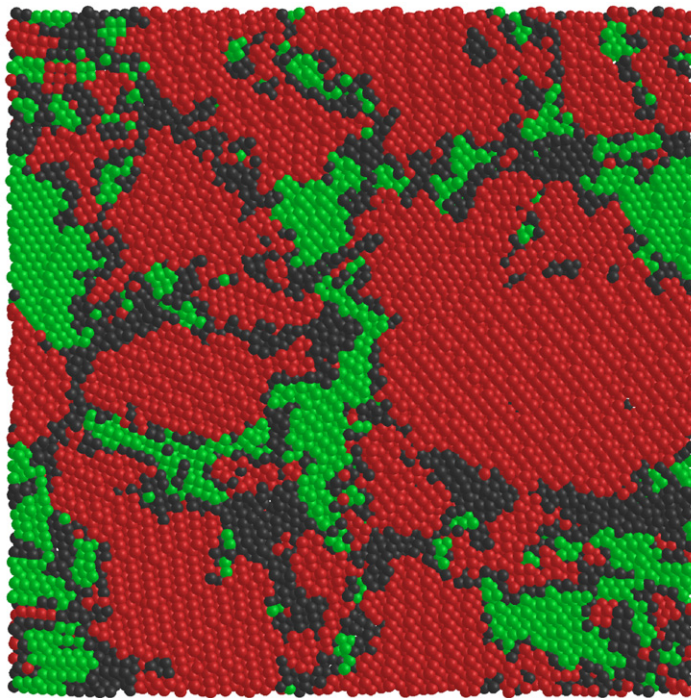


**Figure 9.** Austenite  $\rightarrow$  martensite transformation during severe plastic deformation of a 6 nm diameter Voronoi polycrystal at  $T = 300$  K during cycling with a peak strain of 0.04. Transformation from austenite (green) to martensite (red) starts to nucleate in high shear stress regions of the grain boundaries and—at sufficiently high peak strain levels—propagates throughout the whole polycrystal.

corresponds to a uniform angular distribution ( $n_{nb}$  denotes the number of nearest neighbors). Applying this definition with respect to austenite and martensite as reference structures and defining a threshold (somewhat arbitrarily chosen as 0.225) to discriminate between agreement ( $P_{st} \leq 0.225$ ) and non-agreement ( $P_{st} > 0.225$ ) with that reference structure, maps of martensitic and austenitic regions can be generated (figure 9). From visual inspection under a variety of different conditions, it becomes clear that martensite preferentially nucleates in high shear stress regions in grain boundary proximity and from there—depending on external strain—propagates almost completely into the grains.

## 6. Comparison with experiments and discussion

### 6.1. 1.8 MeV $Kr^+$ irradiation of austenitic single-crystal $Fe_7Pd_3$ films

As described in detail earlier [7, 42], single crystalline 500 nm thick  $Fe_7Pd_3$  films were deposited by molecular beam epitaxy from two independently rate-controlled electron beam evaporators (total deposition rate:  $0.15 \text{ nm s}^{-1}$ ) onto  $1 \times 1 \text{ cm}^2$  sized MgO (001) single-crystal substrates (substrate temperature:  $\approx 1120$  K) using ultrahigh vacuum conditions (base pressure  $3 \times 10^{-9}$  mbar or better). After rapidly cooling down to room temperature with the help of a liquid nitrogen filled cryo shield, films prepared under these conditions reside in the austenite



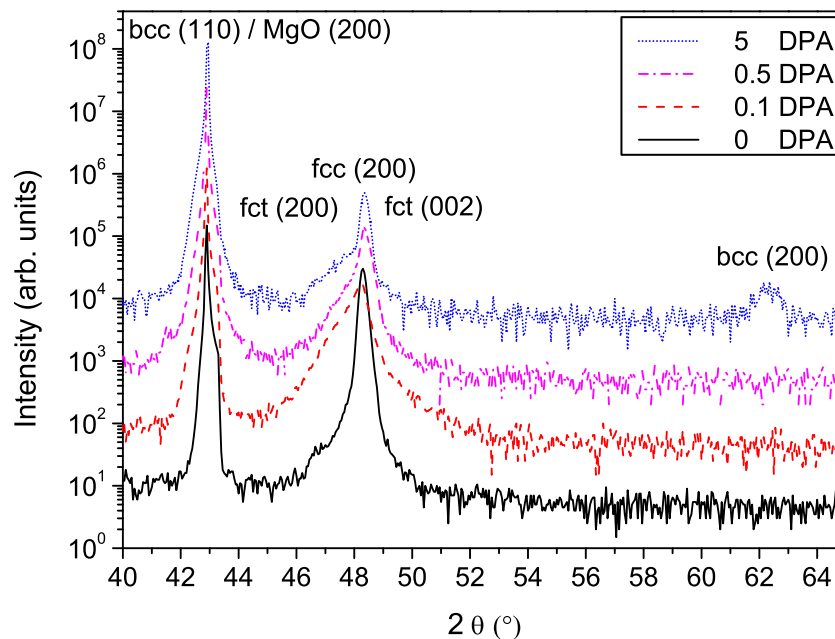


**Figure 10.** XRD measurements confirm an austenite  $\rightarrow$  martensite transition in the course of irradiation of *as prepared* austenite films with 1.8 MeV  $\text{Kr}^+$  ions. The austenite fcc (200) peak decreases with dose while increasing fct (200) peaks and—for 5 dpa—bcc (110) and bcc (200) are identified.

( $\gamma'$ ) phase; similar films have recently been characterized extensively with respect to physical and material properties [5, 7, 42, 43]. Using a diamond saw, each of the substrates is cut into four pieces, three of which are mounted in a high-vacuum chamber onto a Cu block for homogeneous irradiation with 1.8 MeV  $\text{Kr}^+$  ions, while beam heating of the samples was negligible for the applied currents below  $300 \text{ nA cm}^{-2}$  employed here [44]. As a detailed account of the resulting materials and actuation properties is beyond the scope of the present work and will be given elsewhere [45], we currently only focus on experimental confirmation of the theoretically predicted properties, i.e. point defect and disorder-induced austenite  $\rightarrow$  martensite transformation due to an increase of martensite temperature beyond room temperature.

Figure 10 shows modification in crystal structure in the course of ion bombardment, as measured with x-ray diffraction (Cu  $K_\alpha$  radiation). *As-prepared* films reside in the fcc austenitic  $\gamma$  phase. Ion bombardment induces a successive transformation first to fct and then to bct/bcc martensite—as is visible from the corresponding peaks in the x-ray spectrum (figure 10). Minor contributions of some of the variants in martensite can be attributed to film stresses due to substrate constraints. It is also worth emphasizing that the order of magnitude of the transformation dose matches the predictions of our EAM potential reasonably well, thus confirming the underlying model assumptions. Deviations in the exact doses when comparing the present experiments with our model predictions (sections 6.1 and 4) are, in fact, expected because of (i) the simultaneous presence of point defect generation *and* disordering, (ii) recombination, annihilation and agglomeration of point defects, (iii) re-ordering tendencies by atomic transport and (iv) thermal spikes, which are present in experiments but neglected in our model assumptions at this point.

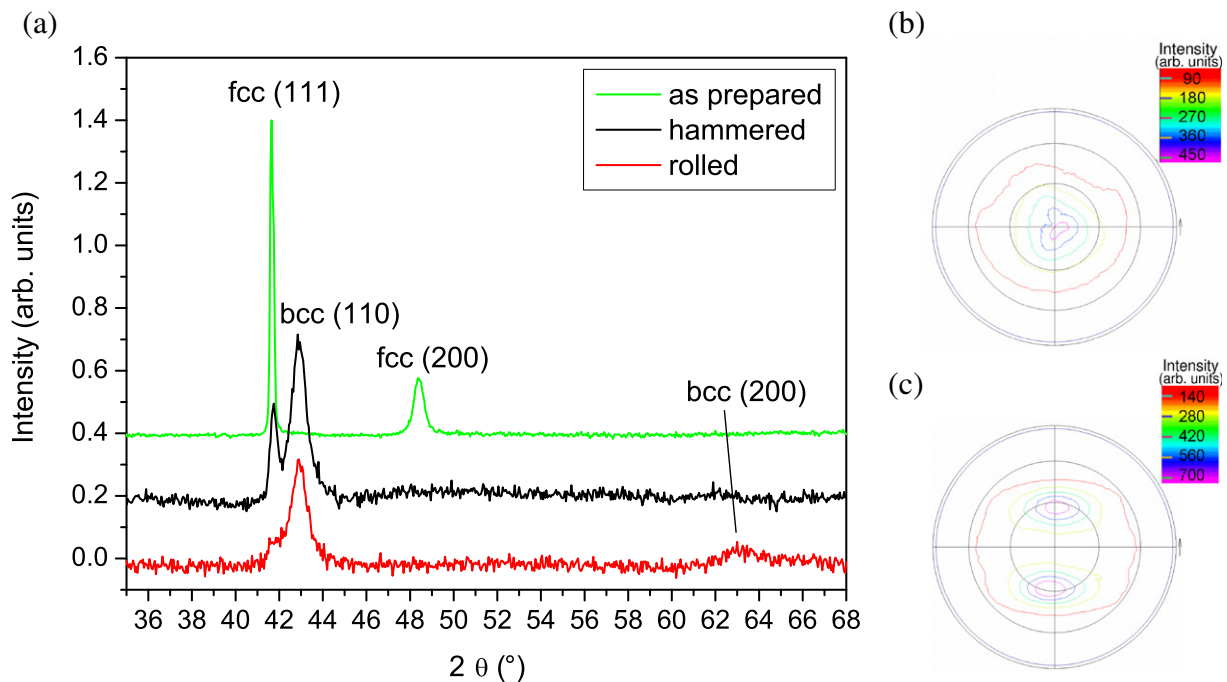


**Figure 11.** (a) *As prepared* austenitic  $\text{Fe}_7\text{Pd}_3$  splats partially and fully transform to bcc martensite during severe plastic deformation by manual hammering and rolling, respectively. As visible in pole figure measurements, rolling of *as prepared* splats (b) is accompanied by development of a crystallographic texture (c).

## 6.2. Severe plastic deformation of $\text{Fe}_7\text{Pd}_3$ splats

To compare the modeling results on SPD with experiments, splat quenching [46] was employed to synthesize polycrystalline  $\text{Fe}_7\text{Pd}_3$  foils of  $\approx 60 \mu\text{m}$  thickness, which *as prepared* reside in the austenite ( $\gamma$ ) phase. Details of the preparation process and the precautions that were taken to ensure high sample homogeneity and purity have been described earlier [9, 47]. Severe plastic deformation of splats was subsequently conducted by (i) hammering and (ii) cold rolling, until the splat thickness was reduced to approximately half of its initial value. Characterization with x-rays (like in section 6.1—figure 11(a)) reveals transformation of (i) large portions and (ii) all of the initially austenitic samples to bcc martensite in the course of hammering and cold rolling, respectively. These findings are in excellent agreement with the predictions of the proposed EAM potential. During severe plastic deformation, crystal quality is significantly reduced—as can be concluded from the dramatic peak broadening in figure 11(a)—while pole figure measurements made before (figure 11(b)) and after (figure 11(c)) cold rolling indicate the development of a rolling texture.

## 7. Conclusions and outlook

Based on the results of *ab initio* calculations, a many-body interatomic potential of the embedded atom method type has been suggested for the highly promising  $\text{Fe}_7\text{Pd}_3$  ferromagnetic

shape memory alloy. Tailored to correctly account for the energetics along the Bain path from bcc martensite to fcc austenite in the fully disordered and ordered lattices, as well as the relative stabilities and lattice constants of the ordered  $L1_0$  and  $L1_2$  phases, it is intended for scenarios which require larger systems and longer simulation times than is feasible with *ab initio* methods. This is demonstrated in three instances, the influence of (i) order/disorder, (ii) point defects as generated during ion irradiation and (iii) severe plastic deformation on phase stability of martensite and austenite. In agreement with experiments, which are also presented, the model predicts that (i) complete disorder favors bcc martensite, while increasing  $L1_2$  ordering shifts tetragonality toward austenite, (ii) insertion of Frenkel pairs, as in ion irradiation, elevates the martensite temperature and (iii) severe plastic deformation of austenite induces a phase change to martensite, while single and poly-crystals quantitatively behave fundamentally differently. More tests—in particular with respect to transferability to different situations, are currently in progress, including the ambition of giving a full thermodynamic account of the temperature-dependent equilibrium short-range order and vacancy density—and the coupling to martensite transformation.

## Acknowledgments

We acknowledge Dr I Claussen for experiments on splats, Professor Dr R S Averback (UIUC) for facilitating  $Kr^+$  ion irradiation as well as Professor Dr Dr h.c. B Rauschenbach for general support. This project was funded in part by the German Federal Ministry of Education and Research (BMBF) through PTJ-BIO 0315883, the European Union/ESF and the Free State of Saxony, Germany; it was partly performed within the Leipzig Graduate School for Natural Sciences ‘Building with Molecules and Nano Objects’ (BuildMoNa) established within the German Excellence Initiative by the DFG.

## References

- [1] Ullakko K *et al* 1996 *Appl. Phys. Lett.* **69** 1966
- [2] Ma J and Karaman I 2010 *Science* **327** 1468
- [3] Webster J, Ziebeck K R A, Town S L and Peak M S 1984 *Phil. Mag. B* **49** 295
- [4] James R D and Wuttig M 1998 *Phil. Mag. A* **77** 1273
- [5] Ma Y, Zink M and Mayr S G 2010 *Appl. Phys. Lett.* **96** 213703
- [6] Cui J, Shield T W and James R D 2004 *Acta Mater.* **52** 35
- [7] Edler T and Mayr S G 2010 *Adv. Mater.* **22** 4969
- [8] Claussen I, Brand R, Hahn H and Mayr S 2012 *Scr. Mater.* **66** 163
- [9] Claussen I and Mayr S G 2011 *New J. Phys.* **13** 063034
- [10] Gruner M E and Entel P 2011 *Phys. Rev. B* **83** 214415
- [11] Mayr S G 2012 *Phys. Rev. B* **85** 014105
- [12] Kato H, Liang Y and Taya M 2002 *Scr. Mater.* **46** 471
- [13] Haasen P 1996 *Physical Metallurgy* 3rd edn (Cambridge: Press Syndicate of the University of Cambridge)
- [14] Daw M S and Baskes M I 1983 *Phys. Rev. Lett.* **50** 1285
- [15] Daw M S and Baskes M I 1984 *Phys. Rev. B* **29** 6443
- [16] Hohenberg P and Kohn W 1964 *Phys. Rev.* **136** B864
- [17] Vanderbilt D 1990 *Phys. Rev. B* **41** 7892
- [18] Rappe A M, Rabe K M, Kaxiras E and Joannopoulos J D 1990 *Phys. Rev. B* **41** 1227
- [19] Blöchl P E 1994 *Phys. Rev. B* **50** 17953

- [20] Giannozzi P *et al* 2009 *J. Phys.: Condens. Matter* **21** 395502
- [21] Perdew J P, Burke K and Ernzerhof M 1996 *Phys. Rev. Lett.* **77** 3865
- [22] Zunger A, Wei S-H, Ferreira L G and Bernard J E 1990 *Phys. Rev. Lett.* **65** 353
- [23] von Pezold J, Dick A, Friák M and Neugebauer J 2010 *Phys. Rev. B* **81** 094203
- [24] Methfessel M and Paxton A T 1989 *Phys. Rev. B* **40** 3616
- [25] Mendeleev M I, Han S, Srolovitz D J, Ackland G J, Sun D Y and Asta M 2003 *Phil. Mag.* **83** 3977
- [26] Voter A F and Chen S P 1987 *Mater. Res. Soc. Symp. Proc.* **82** 175
- [27] Voter A F 1993 *Los Alamos Unclassified Technical Report* LA-UR 93-3901
- [28] Bonny G, Pasianot R C and Malerba L 2009 *Modelling Simul. Mater. Sci. Eng.* **17** 025010
- [29] Massalski T B 1986 *Binary Alloy Phase Diagrams* (Metals Park, OH: American Society for Metals)
- [30] Opahle I, Koepf K, Nitzsche U and Richter M 2009 *Appl. Phys. Lett.* **94** 072508
- [31] Allen M P and Tildesley D J 1990 *Computer Simulation of Liquids* (New York: Oxford University Press)
- [32] Mayr S G 2009 *Phys. Rev. B* **79** 060201
- [33] Mayr S G 2006 *Phys. Rev. Lett.* **97** 195501
- [34] Nose S 1984 *Mol. Phys.* **52** 255
- [35] Hoover W 1985 *Phys. Rev. A* **31** 1695
- [36] Parrinello M and Rahman A 1980 *Phys. Rev. Lett.* **45** 1196
- [37] Kakeshita T, Fukuda T, Terai T, Takeuchi T and Kishio K 2003 *J. Physique IV* **112** 93
- [38] Averback R S and de la Rubia T D 1998 *Solid State Phys.* **51** 281
- [39] Mayr S G and Averback R S 2005 *Phys. Rev. B* **71** 134102
- [40] Van Swygenhoven H 2002 *Science* **296** 66
- [41] Zhu H, Averback R S and Nastasi M 1995 *Phil. Mag. A* **71** 735
- [42] Kühnemund L, Edler T, Kock I, Seibt M and Mayr S 2009 *New J. Phys.* **11** 113054
- [43] Edler T, Hamann S, Ludwig A and Mayr S G 2011 *Scr. Mater.* **64** 89
- [44] Mayr S G and Averback R S 2001 *Phys. Rev. Lett.* **87** 196106
- [45] Arabi-Hashemi A, Brand R A, Hahn H, Averback R S and Mayr S G 2012 in preparation
- [46] Duwez P, Willens R H and Klement W 1960 *J. Appl. Phys.* **31** 1136
- [47] Kock I 2010 *PhD Thesis* University of Göttingen, Germany <http://webdoc.sub.gwdg.de/diss/2010/kock/>